1 A Molecular Simulation Study on Transport Properties of FAMEs in High-Pressure Conditions

Cheng Chen [1], Daniel Mira [2], Xi Jiang [1]*

[1] School of Engineering and Materials Science, Queen Mary University of London, Mile End Road, London E1 4NS, UK

[2] Barcelona Supercomputing Center (BSC-CNS), Barcelona, Spain

* Corresponding author. Email: xi.jiang@qmul.ac.uk

Abstract

Transport property prediction of fatty acid methyl esters (FAMEs) is essential to its utilisation as biodiesel and biolubricant which can work under high-pressure conditions. Equilibrium molecular simulation is performed to study the viscosity, diffusivity, density and molecular structure dynamics at conditions up to 300 MPa. Among the transport properties, convergence of the viscosity needs a sufficiently large number of independent replications of the simulation. The system size effect on diffusion coefficient should be taken into consideration in fitting the Stokes-Einstein relation. The capability of three different force fields on predicting transport properties is evaluated in terms of the united-atom molecular model and all-atom molecular model. The solidification of FAMEs under high pressure occurs with parallel molecular alignment. The spatial inhomogeneity results in the breakdown of Stokes-Einstein relation. A hybrid effective hydrodynamic radius is established on the linear relation between experimental viscosity and diffusion coefficient in molecular simulation. This provides a predictive method to estimate viscosity from molecular diffusion coefficient over a broad range of conditions provided that Stokes-Einstein relation applies.

Key words: fatty acid methyl ester, biodiesel, transport property, molecular dynamics, high pressure, solidification

Nomenclature

Latin letters

A, B, C	Fitting parameter
c_d	Drag coefficient
C_v	Correlation function of velocity
C_p	Correlation function of pressure tensor
C_{Rot}	Rotational correlation function
D	Diffusion coefficient
E	Potential energy
F	Parameter in Fourier series
f	Newton force
i, j, k, l	Atom index
k	Force parameter in bond and angle energy formula
k_B	Boltzmann constant
K_n	A Kernel function
L	Length of simulation box
l	Effective bond length
M	Molecular mass
N	Number of molecules/atoms
n_b	Number of beads
P	Pressure/pressure tensor
P_c	Critical pressure
P_n	n^{th} order of Legendre polynomial
q	Partial charge on atom
R	Radius; gas constant
r	Distance between two atoms
$\boldsymbol{R}$	Vector between two atoms
R_{ee}	End-to-end atom distance
R_{eff}	Effective hydrodynamic radius
R_g	Gyration radius
S	Collective variable of SMAC
T	Temperature
t	Time
T_b, T_c, T_m, T_g	Boiling temperature, Critical temperature, Melting temperature, Glass
σ	The distance at which the LJ potential energy is zero; switching function
τ	Fitting parameter
θ	Bond angle
ξ	A certain physical property related to transport property

Subscripts/superscripts

a	Two-bond angle
b	Bond stretching interaction
α, β	A component of axis in Cartesian coordinates
d	Dihedral angle
f	Fast decay
nb	Non-bonded interactions
Rot	Rotational motion
s	Slow decay
Tra	Translational motion

Abbreviations

AA	All-atom
AARD	Average Absolute Relative Deviation
ACF	Autocorrelation Function
CHARMM	Chemistry at Harvard Macromolecular Mechanics
DCN	*n*-Decane
DDC	*n*-Dodecane
EMD	Equilibrium Molecular Dynamics
FAME	Fatty Acid Methyl Ester
GK	Green-Kubo
HTHP	High-Temperature High-Pressure
HXD	*n*-Hexadecane
LJ	Lennard-Jones
MDC	Methyl Decanoate
MD	Molecular Dynamics
MMR	Methyl Myristate
MSD	Mean Square Displacement

	transition temperature		
V	Volume of box	NEMD	Non-Equilibrium Molecular Dynamics
v	Velocity	NPT	Isothermal-Isobaric (fixed atom numbers, pressure, and temperature)
x, y, z	Cartesian coordinate	NVT	Canonical ensemble (fixed atom numbers, volume, and temperature)
Greek letters		OPLS	Optimized Potentials for Liquid Simulations
		OTN	*n*-Octane
α, β	Fitting parameter	PACF	Autocorrelation Function of Pressure Tensor
χ	A certain transport property	PME	Particle-Mesh Ewald
ε	Depth of the LJ potential well	SD	Standard Deviation
ε_0	Permittivity of vacuum	SE	Stokes-Einstein
η	Viscosity	SED	Stokes-Einstein-Debye
Γ	Gamma function	SMAC	Solid Molecule Angle Criteria
ι	A dimensionless constant determined by an Ewald-like summation of a periodic lattice	TraPPE	Transferable Potentials for Phase Equilibria
ω	Frequency	TDM	Time Decomposition Method
ϕ	Torsion angle	UA	United-atom
ψ	Switching function	UB	Urey-Bradley
ρ	Density	VACF	Velocity Autocorrelation Function

2 Background

Fatty acid methyl esters (FAMEs) are the primary components of biodiesel which can be produced from transesterification of feedstocks like vegetable oils, animal fats and algae. Biodiesel is a renewable fuel which is regarded as a sustainable alternative of petrodiesel [1]. Polyol esters derived from different chemically modified FAMEs can also be used as biodegradable lubricant. For example, Polyol esters featuring one or more ester groups in a molecule as well as long and branched molecular architecture are used as refrigeration lubricants in a compressor [2]. The properties of the produced biodiesel and biolubricant must conform to the standards of quality specifications before the large-scale commercial application. In general, transport properties of viscosity and density are two of the most important properties of fuels and lubricants, because they are inherently linked to the fuel injection, atomisation processes and lubricant rheology.

Unlike fatty acids which would cause corrosion of metal structures, FAME is not subject to corrosion. The processes of heat, mass and momentum transfer in the utilisation of renewables such as FAMEs is controlled by the macroscopic properties of the fuel, reflecting different molecular structures of the chemicals. FAME molecules are the combination of hydrocarbon chains and ester function groups. Biodiesel is a mixture of FAMEs with different chain lengths ranging from C6:0 to C24:0 (in terms of lipid numbers) and different degrees of unsaturation ranging from C18:1 to C18:3 [3]. The methyl ester constituents of biodiesel vary significantly depending on the feedstock used for production. Physicochemical properties of FAMEs such as density, viscosity, and oxidative stability *etc*., show strong correlation with the molecular structure configurations.

The molecular structures of two representative unsaturated FAMEs of different chain lengths, *i.e*. Methyl Decanoate (MDC, C10:0) and Methyl Myristate (MMR, C14:0), are selected in this study. This is because the existing isothermal high-pressure experimental data of MDC and MMR performed by Habrioux *et al*. [4, 5] can be used for validation of the MD simulation. Basic physical properties of molecular weight, fusion temperature and boiling temperature of corresponding *n*-alkanes and branched alkanes are listed in **Table 1** for comparison. FAMEs and *n*-alkanes with the same chain length have similar fusion temperature, which is 20% higher than that of branched alkanes. Boiling point of FAMEs is higher than that of normal alkane and branched alkanes. Both FAMEs and alkanes with longer chain length have higher fusion temperature and boiling temperature.

Table 1. Properties of FAMEs and alkanes for comparison: molecular weight (M), and phase change data of fusion or melting temperature (T_m), boiling temperature (T_b), critical temperature (T_c) and critical pressure (P_c) [6, 7].

FAMEs and alkanes	M (g/mol)	T_m (K)	T_b (K)	T_c (K)	P_c (MPa)
Methyl Decanoate (MDC: $C_{11}H_{22}O_2$)	186.29	260.40	497.20	689.05	1.97
Methyl Myristate (MMR: $C_{15}H_{30}O_2$)	242.40	291.24	596.20	747.00 [7]	1.57 [7]
n-Octane (OTN: C_8H_{18})	114.23	216.60	398.77	569.32	2.50

n-Decane (DCN: $C_{10}H_{22}$)	142.29	245.25	447.27	617.70	2.10
n-Dodecane (DDC: $C_{12}H_{26}$)	170.33	263.50	489.00	658.10	1.82
n-Hexadecane (HXD: $C_{16}H_{34}$)	226.44	291.00	554.00	722.00	1.40
2,2,4,6,6-pentamethylheptane (PMH: $C_{12}H_{26}$)	170.33	206.00	451.00	-	-
2,2,4,4,6,8,8-Heptamethylnonane (HMN: $C_{16}H_{34}$)	226.44	-	513.20	692.00	1.57

Transport properties of liquid fuels and their dependencies on pressure and temperature play an essential role in the development and operation of relevant chemical engineering infrastructures including fuel processing and utilisation. It is acknowledged that biodiesel has higher viscosity, density and surface tension than diesel, which would dramatically affect the engine operation and the subsequent combustion emission. Biolubricants present some attractive properties such as low toxicity, biodegradability, low friction and wear characteristics, *etc.* [8]. Reliable methods on accurate prediction of the transport property of liquid fluids are lacking particularly for organics with complexed molecular structures [9]. The high-pressure induced solidification and crystallization of FAMEs observed in experiments [10, 11] make the viscosity prediction in high-pressure conditions very challenging. The modern common-rail injection system has been tested in the pressure above 300 MPa [11, 12]. Moreover, lubricated machine components, such as gears and bearings, generally operate in elastohydrodynamic lubrication regime where lubricants are compressed in concentrated contacts and the pressure is extremely high which can be up to giga-pascals [2].

Recently, advances in molecular dynamics (MD) simulation of both equilibrium and nonequilibrium make it a promising method in understanding phase transition and property prediction. To be specific, in the nonequilibrium molecular dynamics (NEMD) simulation, shear viscosity depends on the shear rate for non-Newtonian liquids and should be extrapolated to the zero shear rate. Nie *et al*. [13] reviewed the application of MD simulation to transport property prediction of working fluids in supercritical conditions. It was recommended that equilibrium molecular dynamics (EMD)

with Green-Kubo (GK) method is more appropriate for viscosity calculation than NEMD method. Falk *et al.* [14] and Kondratyuk *et al*. [15-17] studied the rheology of alkane lubricant at pressures up to 1000 MPa. It was manifested that it is still feasible to use EMD to study liquid properties of hydrocarbon even under extreme pressures. However, the prerequisite of non-solidification was not discussed in these studies. Wang *et al*. [18] and Yang *et al*. [19] studied the viscosity of JP-10, *n*-decane, *n*-undecane and *n*-dodecane using EMD simulation at isobaric sub- to supercritical conditions. After comparing with the NIST data, it was found that force field parameters greatly affected the accuracy. To assess the effect of molecular configurations on transport properties, Chae *et al*. [20, 21] studied the mutual diffusion coefficients of linear alkane and the corresponding isomers in nitrogen using EMD with GK method. It was found that the radius of gyration can be used as the index to determine accurate values of the diffusion coefficients of alkane isomers.

There has not been an in-depth molecular study on the properties of FAMEs in high-pressure conditions, to the best of our knowledge. In addition, there has not been a discussion on the convergence of viscosity and the system size effect on diffusion coefficient. The possible solidification of FAMEs in high pressures has not been investigated in existing modelling/simulation studies. Overall, it is expected that MD modelling becomes routinely used to bridge the fundamental knowledge / physical insight and practical use of fuels and lubricants with complicated molecular structures, considering that force fields (which are crucial to the simulation accuracy) and molecular simulations are becoming increasingly more accurate and computationally more affordable.

In this study, EMD simulation is performed to compute the transport property of two typical FAME molecules (MDC and MMR) at pressures up to 300 MPa. The paper is organised as follows: The methodology of transport property prediction in EMD is introduced in section **2**. It includes outlines of the two methods, *i.e.*, the GK relation and Einstein relation for calculations of viscosity and diffusion coefficient. The potential energy formulas of force field and the detailed EMD simulation setup are also introduced in this section. The results are demonstrated in section **3**,

including the effect of pressure, system size and force field parameters on the convergence and accuracy of transport properties. The correlation between viscosity and diffusivity, *i.e*. the Stokes-Einstein relation, is also demonstrated in this section. In section **4**, the high-pressure induced solidification and the consequent violation in property prediction are discussed. Finally, a predictive method is established according to the correlation between experimental viscosity and EMD diffusivity.

3 Transport property prediction in EMD

3.1 The Green-Kubo and Einstein method

The transport property (χ) can be calculated from an EMD simulation, *via* correlation with specific variable ξ by the Einstein equation or its time derivation $\dot{\xi}$ by the GK equation [22, 23]. In the GK method, transport property is related to the running integral of the autocorrelation function (ACF) for $\dot{\xi}(t)$:

$$\chi = \int_0^\infty \langle \dot{\xi}(t_0)\dot{\xi}(t_0+t)\rangle_{t_0} dt. \quad (1)$$

An equivalent expression for χ is known as the Einstein formula *via* mean-square of variable ξ:

$$\chi = \lim_{t\to\infty} \frac{\langle(\xi(t_0)-\xi(t_0+t))^2\rangle_{t_0}}{2t} = \frac{1}{2}\lim_{t\to\infty}\frac{d}{dt}\langle(\xi(t_0)-\xi(t_0+t))^2\rangle_{t_0}. \quad (2)$$

Although the simulation setup and computational cost are essentially the same for these two approaches, in practice one method is often preferred depending on the properties being estimated. For viscosity, the GK method is related to the autocorrelation function of pressure tensor (PACF):

$$\eta = \frac{V}{k_B T}\int_0^\infty \left(\left\langle P_{\alpha\beta}(t)P_{\alpha\beta}(0)\right\rangle\right) dt, \quad (3)$$

where V is volume, k_B is Boltzmann constant, T is temperature, $P_{\alpha\beta}$ represents the $\alpha\beta$ components of the pressure tensor, α, β is any two of the x, y or z Cartesian coordinates. Shear viscosity is a collective property as the GK formulation consolidates the contributions of all the atoms into a single

autocorrelation function. To improve the convergence, it is common to include multiple terms from the pressure tensor:

$$\eta = \frac{V}{10k_BT}\int_0^\infty \left(\left\langle \sum_{\alpha\beta} P_{\alpha\beta}(t)P_{\alpha\beta}(0)\right\rangle\right) dt, \quad (4)$$

where the factor of 10 results from assigning weighting factor of 3/3 and 4/3 for each of the six off-diagonal ($\alpha \neq \beta$) terms and the three diagonal terms [23]. It should be noted that the ACFs of the three off-diagonal elements of the pressure tensor are expected to be equivalent/dependent, attributed to the isotropy of the system. The pressure tensor is calculated from the following equation:

$$P_{\alpha\beta}(t) = \frac{1}{V}\left(\sum_{i=1}^{N} M_i v_{i_\alpha} v_{i_\beta} + \sum_{i=1}^{N-1}\sum_{j>1}^{N} r_{ij_\alpha} f_{ij_\beta}\right), \quad (5)$$

where M_i is the mass of a molecule i, N is the number of molecules, $v_{i\alpha}$ and $v_{i\beta}$ are the velocity components of a molecule i in the α and β-directions, and r and f represent the displacement and force between two molecules, respectively.

The Einstein equation connects the self-diffusivity to the particle displacement and can average over the number of the particles. Diffusion coefficient of particles in three dimensional systems is calculated using:

$$D_{self} = \lim_{t\to\infty} \frac{1}{6N_i t}\left\langle \sum_{j=1}^{N_i} \left(r_{j,i}(t) - r_{j,i}(0)\right)^2 \right\rangle, \quad (6)$$

where $r_{j,i}(t)$ is the position of the j^{th} molecule of species i at time t, and N_i is the number of molecules of species i in the system. The particle mean square displacement (MSD) grows linearly with the time for a sufficiently large value of t [24]. In homogeneous system, $D_{xx}=D_{yy}=D_{zz}$ [22].

Besides the translational diffusivity, molecular motions also lead to changes in molecular orientations. Rotational motion and reorientation of molecules can be characterised by an end-to-end vector, *i.e.*, $\boldsymbol{R}$ defined by the coordinates of the terminal carbon atoms. Relaxation time is determined by the ACF of angle θ between the end-to-end vector of a given molecule:

$$t_{Rot}(t) = \int_0^\infty P_n(\cos\angle(\boldsymbol{R}(t), \boldsymbol{R}(0))\mathrm{d}t, \quad (7)$$

where P_n is the n^{th} order Legendre polynomial.

3.2 Modelling system setup

Three different force fields, *i.e.*, TraPPE [25], CHARMM [26] and OPLS [27] are selected to predict the transport properties of FAMEs. In MD simulation, the energy of non-bonded interactions between atoms are described based on the Coulomb potential and the 12-6 Lennard-Jones (LJ) potential:

$$E_{nb}(r_{ij}) = \frac{q_i q_j}{4\pi\varepsilon_0 r_{ij}} + 4\varepsilon_{ij}\left(\left(\frac{\sigma_{ij}}{r_{ij}}\right)^{12} - \left(\frac{\sigma_{ij}}{r_{ij}}\right)^{6}\right), \quad (8)$$

where r_{ij} is the distance between two atoms i and j, q_i and q_j are the partial charges on the atoms, ε_0 is the permittivity of vacuum, σ_{ij} is the van der Waals radius, and ε_{ij} is the well-depth for this atom pair. The LJ pair coefficients for interactions between unlike atoms are computed using arithmetic average and geometric average: $\sigma_{ij} = (\sigma_{ii} + \sigma_{jj})/2$ and $\varepsilon_{ij} = (\varepsilon_{ii}\varepsilon_{jj})^{1/2}$.

Intramolecular interaction of bond stretching is represented by a harmonic potential:

$$E_b(r_{ij}) = \frac{1}{2}k_{ij}^b(r_{ij} - b_{ij})^2. \quad (9)$$

Bond-angle vibration between a triplet of atom is also represented by a harmonic potential:

$$E_a(\theta_{ijk}) = \frac{1}{2}k_{ijk}^\theta(\theta_{ijk} - \theta_{ijk}^0)^2. \quad (10)$$

In CHARMM force field, an Urey-Bradley correction term is included [26]:

$$E_a^{UB}(\theta_{ijk}) = \frac{1}{2}k_{ijk}^{UB}(r_{ik} - r_{ik}^0)^2. \quad (11)$$

In TraPPE and OPLS force fields, proper dihedral angles separated by the three bonds are represented by the cosine terms of a Fourier series:

$$E_d^F(\phi_{ijkl}) = \frac{1}{2}\left(\sum_{n=1}^{4} F_n(1 + (-1)^{n+1}\cos(n\phi))\right). \quad (12)$$

In CHARMM force field, dihedral potential is expressed as:

$$E_d(\phi_{ijkl}) = k_\phi(1 + \cos(n\phi - \phi_s)). \quad (13)$$

The OPLS all-atom (AA) force field was parameterized for simulation of organic molecules and peptides. The pair potential for atoms is separated by three bonds or more within a molecule, *i.e.*, 1-4 interactions are scaled down by the "fudge factor" of 0.5. In this study, the optimised OPLS parameters for esters and long alkanes (LOPLS) are adopted [28, 29]. CHARMM is an all-atom force field which is widely used in biochemistry applications, in particular simulation of lipid membranes for which dedicated membrane builder tools are available. Force field parameters of CHARMM36 [30] are used and topology files are generated from CHARMM General Force Field [26]. TraPPE-UA is a united-atom (UA) potential, which is computationally more efficient than LOPLS-AA and CHARMM-AA. In TraPPE force field, all bond length is fixed, and intramolecular nonbonded 1-4 interactions are already considered in torsion energy. The parameters of ester function group are adopted from the work of Kamath *et al.* [31].

All EMD simulations are performed in the GROMACS molecular simulation package [32]. The initial boxes are constructed by distributing molecules randomly in a relative larger box to avoid overlap as shown in **Fig 1 (a)**. MD systems are relaxed *via* the steepest descent energy minimization to ensure the system has no steric clashes or inappropriate geometry. The minimization is considered as converged when the maximum force on any atom is less than 1000 $KJ \cdot mol^{-1} \cdot nm^{-1}$. Equilibration run is performed for 500 ps in *NPT* ensemble (isothermal-isobaric, constant Number of particles, Pressure, and Temperature) to compress the system to the desired pressure and density as shown in **Fig 1 (b)**. The Parrinello-Rahman barostat is used for pressure coupling with the compressibility set as 4.5E-5/bar. Temperature is coupled using the velocity rescaling method. Production run of 0.5-100 ns in *NVT* (isothermal-isochoric, constant Number of particles, Volume, and Temperature) ensemble is then followed for data collection.

The initial velocity of molecule is generated according to Maxwell distribution of temperature with random seed. Neighbour searching was performed using the Verlet scheme, with a list created

every one step using a length of 1.4 nm. The cut-off distance of LJ potential is 1.4 nm. The long-range electrostatic interactions were calculated using the fourth order particle-mesh Ewald (PME) algorithm with a cut-off distance of 1.4 nm in real space. The size of FFT (fast Fourier transform) grid in reciprocal space of PME is 0.12 nm. The periodical boundary conditions in all directions are used in all simulations. The time step is set as 1 fs for all simulations. LINCS constraint-algorithm is used to fix all the bonds in TraPPE force field and C-H bonds in LOPLS and CHARMM force field.

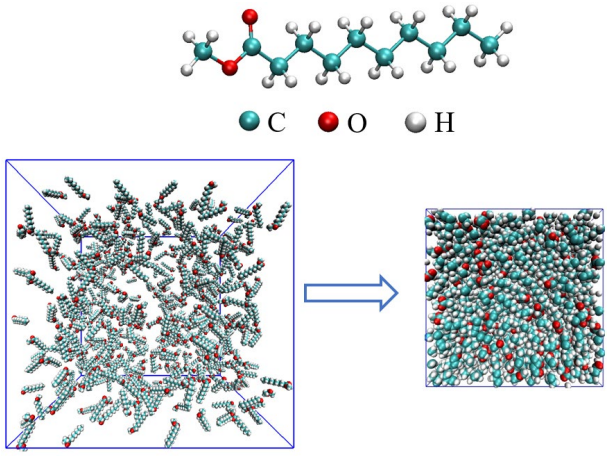

Fig 1. Equilibrium run and compression of the EMD system containing 500 MDC molecules: (a) snapshot of the initial box with molecules distributed randomly; (b) snapshot of box after 500 ps simulation in *NPT* ensemble at 298.15 K and 0.1 MPa.

4 Results

4.1 Viscosity

Systems configured in **Fig 1** with TraPPE force field are used to study the pressure effect on viscosity and diffusivity at 298.15 K. Normalized PACF and time evolution of viscosity at 0.1 MPa are shown in **Fig 2 (a)**. Pressure effect on viscosity is shown in **Fig 2 (b).** Pressure tensor is dumped every 5 fs which is frequent enough to accurately calculate the time integration. In **Fig 2 (a)**, normalized PACF decays rapidly, reaching the minimum at 0.04 ps followed by the fluctuation around zero. Shear viscosity reaches the first plateau at 74 ps, and sustains until 178 ps during which it

remains stable with an average value of 1.26 cP. In the time period of 200-500 ps, viscosity shows appreciable rise and fall with the maximum value of 1.77 cP at 270 ps and minimum value of 0.87 cP at 391 ps. It was recommended that the estimation of viscosity should be made at the time shortly after $\eta(t)$ has reached the plateau instead of longer correlation times [33]. However, it is not feasible to apply this criterion to distinguish the effect of pressure on viscosity. As shown in **Fig 2 (b)**, the plateau in each curve cannot be easily identified. At around 100 ps, the plateau value of $\eta(t)$ for 0.1 MPa is higher than those for 1 MPa and 10 MPa, which does not reflect the physical impact of pressure on viscosity. There is no identifiable plateau for $\eta(t)$ at 100 MPa, as it reaches the local maximum value at 60 ps and decreases quickly. It inevitably results in uncertainty if the plateau values are identified directly using distributions shown in **Fig 2 (b)**.

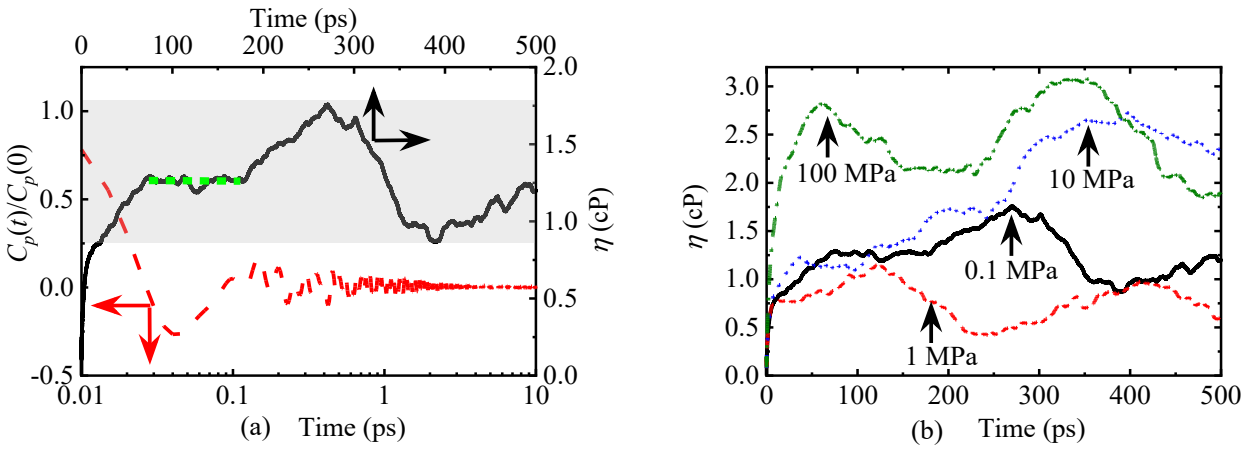

Fig 2. (a) Viscosity of MDC at 298.15 K and 0.1 MPa using the GK method, where viscosity is indicated by solid black line, and normalized ACF of P_{xy} is shown in dashed red line; the shaded region indicates the largest fluctuation range, green dotted line indicates the average value of the first plateau, the arrows indicate the corresponding axis; (b) the effect of pressure on the convergence of viscosity.

Identifying the plateau region of the running integration without introducing the numerical uncertainty or deviation is often hampered by the noisy tail of the ACF. To eliminate the tail, one can decompose the PACF by fitting it to the Kohlrausch-Williams-Watts stretched exponential function

228 [22]:

229 $$\frac{C_p(t)}{C_p(0)} = A\mathrm{e}^{-(t/\tau_s)^{\beta_s}} + (1-A)\cos(\omega t)\,\mathrm{e}^{-(t/\tau_f)^{\beta_f}}, \qquad (14)$$

230 where ω is the frequency of rapid pressure oscillations (mainly due to bonded forces in molecular
231 simulations), τ_s and β_s are constants for slow relaxation, τ_f and β_f are the time constant and exponent
232 of fast relaxation. Parameter A is the pre-factor that determines the weight between the fast and slow
233 relaxations. The results from the fitting are shown in **Fig 3 (a)**. The running integral of the fitting
234 function can be used to compute the viscosity.

235 For highly viscous liquids, another approach to improve convergence is the time decomposition
236 method (TDM) proposed by Zhang *et al.* [34] by fitting the running integral. In TDM, a series of
237 independent and shorten trajectories are obtained in *NVT* simulation with the same system
238 configuration but different random seeds for initial velocity distribution. The averaged running
239 integral as a function of time is also fitted to a double stretched exponential functions expressed as:

240 $$\eta(t) = A\alpha\tau_1\left(1-\mathrm{e}^{-t/\tau_1}\right) + A(1-\alpha)\tau_2\left(1-\mathrm{e}^{-t/\tau_2}\right), \qquad (15)$$

241 where A, α, τ_1, and τ_2 are the fitting parameters. When the standard deviation of the replicated running
242 integral is equal to 40% of the averaged $\eta(t)$, it is the time range over which the running integration
243 should be fitted.

244 The mean value of 40 independent replicated running integrals is shown in **Fig 3 (b)**, with the
245 fitted viscosity equal to 1.45 cP. Averaged viscosity reached the plateau at 300 ps with the value of
246 1.41 cP. The minimum value of the averaged viscosity is 1.14 cP in 852 ps. The fluctuation of the
247 averaged viscosity in the late stage still exists but behaves much better than the noisy $\eta(t)$ curve in
248 **Fig 2**. Although the result of viscosity obtained by fitting PACF shows more rapid and stable
249 convergence compared with the result obtained by fitting to the running integral, significant
250 underestimation is demonstrated. Standard deviation as shown in **Fig 3 (b)** increases as a power
251 function of time due to the accumulation of the random noise at long times in the correlation function.

The averaged plateau value of single run in **Fig 2 (a)** is close to the TDM result. It should be noted that the standard deviation between 74 ps and 178 ps ranges from 0.24 cP to 0.44 cP which indicates significant randomness of the value derived from the single run. In the following study, all viscosities are calculated using the TDM method with 40 statistically independent trajectories.

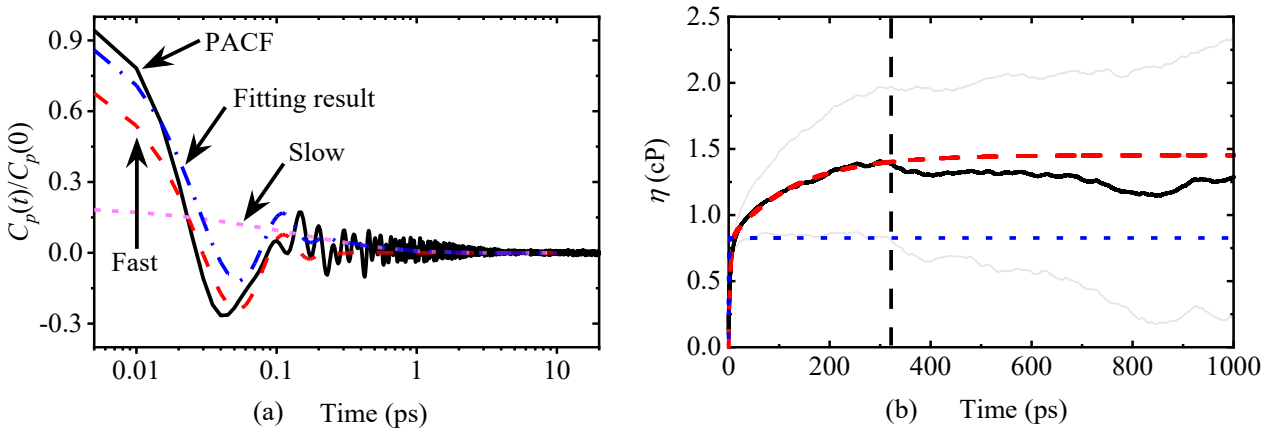

Fig 3. (a) Decomposition and fitting of PACF; (b) viscosity comparison obtained by fitting the running integral and PACF, where solid black line is the averaged viscosity value of 40 independent replicates with standard deviation indicated in the shaded area, red dashed line indicates the fitted value according to Equation (15), blue dotted line is the integration of fitted PACF, black dashed line indicates the time when standard deviation is equal to 40% of the averaged viscosity.

4.2 Diffusivity

Unlike viscosity, diffusion coefficient has less intrinsic uncertainties [35]. It is much easier to obtain accurate self-diffusivity as it describes the motion of individual molecules and the accuracy of statistics is improved by averaging over all particles in the system. The velocity autocorrelation function (VACF) and MSD of molecule centre of mass are shown in **Fig 4**. Oscillatory behaviour of VACF of monatomic LJ fluid is used to identify the Frenkel line of dynamic crossing between gas-like and liquid-like regime in supercritical conditions [36]. VACF of gas decays monotonically in an exponential function. VACF of solids and liquids near the melting temperature has both oscillatory and decaying components due to the cage effect described in cell theory [37, 38]. The negative region

of VACF is typical for liquids and dense gases when rebounding collisions are more frequent than scattering collisions [22, 39]. When pressure increases, the minimum of VACF deepens and shifts to smaller times. Same as the GK method in calculation of viscosity, tail effect would introduce considerable noise in integration of VACF, and it is a trade-off in determining the simulation length of VACF [22]. Diffusion coefficient using the Einstein method by linear regression of MSD is used more widely in MD simulations. In order to avoid the influence of anomalous ballistic diffusion in the initial stage which shows a non-linear relationship between MSD and time, linear fit is performed in the middle region between 100 ps and 900 ps. Atom position data is dumped every 0.1 ps for the observation of the initial ballistic diffusion process.

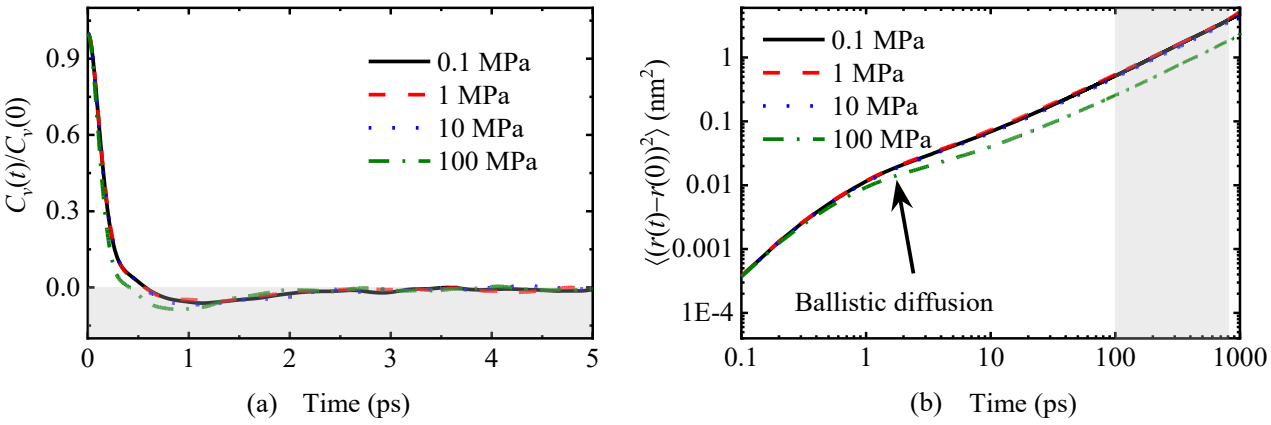

Fig 4. (a) Normalized VACF of MDC centre of mass at different pressures, where shaded area indicates negative values; (b) MSD of MDC centre of mass, where the shaded area is used in the linear regression.

The scaling law of system size must be taken into account to achieve accurate estimates of self-diffusivity [40-43]. Finite size effect of self-diffusivity depends on the hydrodynamic radius of diffusing molecule with respect to the size of the simulation box [40]. Diffusion coefficients of MD systems with different configurations of molecular numbers are shown in **Fig 5**. Linear dependence of self-diffusion coefficient on the number of molecules in the form of $1/N^{1/3}$ (N is the number of molecules in the system) was observed. Self-diffusion coefficient of infinite system size, *i.e.*, D^{∞} is

obtained by the linear fitting and extrapolation. D^{∞} is 5-10% higher than self-diffusion coefficient of system with 500 molecules. Applying an analytical correction term using the following equation derived by Yeh and Hummer [42] is also a feasible approach for to obtain D^{∞}:

$$D_{self}^{\infty} = D_{self}^{MD} + \frac{k_B T \iota}{6\pi\eta L}, \tag{16}$$

where ι is a dimensionless constant equal to 2.837297 for periodic lattice. It was verified that Yeh-Hummer correction results have excellent consistency with the extrapolated infinite self-diffusion coefficient [41, 43]. Finite-size effect on viscosity is generally negligible [22]. It was confirmed that there was no dependence on the system size for the shear viscosity of glymes at 400 K and 30 bar using TDM [41].

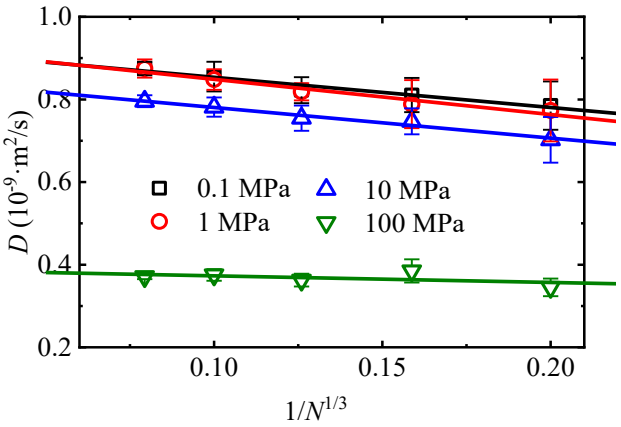

Fig 5. System size effect on diffusion coefficient, where error bars are calculated from 40 independent trajectories and solid lines are linear regression results.

The result of normalized rotational correlation function using different orders of Legendre polynomial of the angle between the end-to-end vectors is shown in **Fig 6 (a)**. Different orders of rotational dynamics of P_1, P_2 and P_3 correlation function correspond to different experimental measurement techniques like spectral band shapes measured in infrared absorption, nuclear magnetic resonance and polarized Raman spectra [44]. The rotational correlation function of P_1, P_2 and P_3 decays to zero at time instants of 512 ps, 185 ps and 96 ps respectively. The longest orientation relaxation time is often employed to determine the duration length of trajectory for accurate viscosity

estimation in single run and the plateau region for data interception in viscosity curve [23]. The effect of pressure on molecular reorientation is shown in **Fig 6 (b)**. The rotational correlation function decays slower in higher pressure conditions indicating longer relaxation time. To evaluate the molecule relaxation time, rotational correlation function was approximated by the sum of two stretched exponential function which corresponds separately to the conformational dynamics and reorientation of overall molecules as a rigid body [14, 33]:

$$\frac{C_{Rot}(t)}{C_{Rot}(0)} = A\mathrm{e}^{-(t/\tau_s)^{\beta_S}} + (1-A)\mathrm{e}^{(t/\tau_f)}. \quad (17)$$

After integrating from t=0 to t=∞, we obtain the correlation time which is given analytically by the gamma function Γ:

$$t_{Rot} = A\tau_s \frac{1}{\beta_s}\Gamma\left(\frac{1}{\beta_s}\right) + (1-A)\tau_f. \quad (18)$$

The results of relaxation time are listed in **Table 2**. Relaxation time increased significantly when pressure was increased to 100 MPa. The characteristic decay times for different values of n can be related by the Debye rule as $t_{Rot\_n}/t_{Rot\_(n+1)}=(n+2)/n$ [33]. Therefore, in the case of isotropic rotational diffusion, a value of 3 for ratio of t_{Rot_1}/t_{Rot_2} and value of 6 for ratio of t_{Rot_1}/t_{Rot_3} is expected. Our results in **Table 2** agree well with this relation, indicating that polynomials of correlation functions with different orders will lead to comparable results. The correction term for system-size scaling effect on rotational diffusion should be extremely small as it is in linear relationship with the inverse value of box volume [40]. So, the system size effect on rotational relaxation time is ignored in the following study.

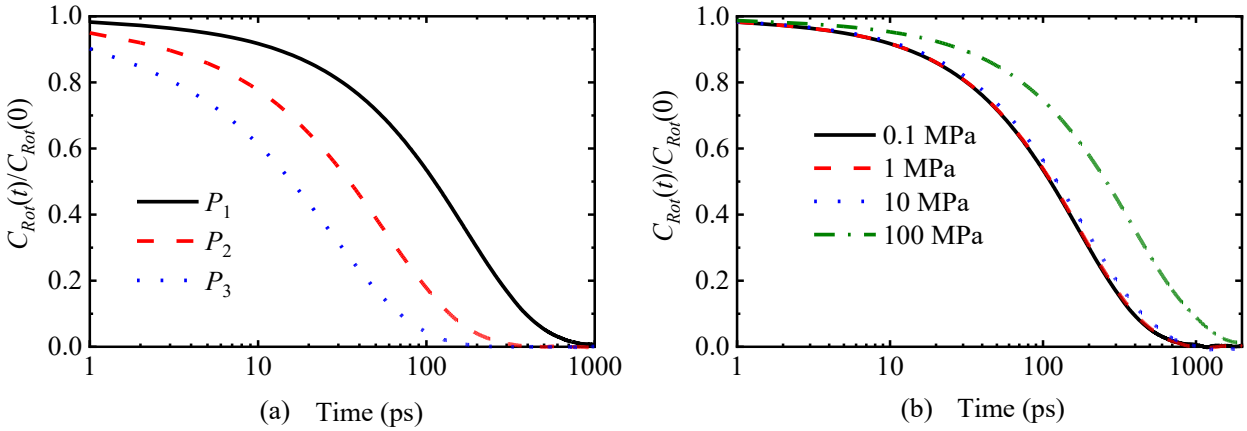

328

329 **Fig 6.** (a) Normalized ACF of MDC molecule end-to-end vector, where P_1 is the first order Legendre
330 polynomial of the angle of the vector; (b) effect of pressure on molecule reorientation using the P_1
331 function.

332 **Table 2.** Different orders of rotational relaxation time of MDC at different pressures, averaged over
333 5 independent trajectories.

P (MPa)	t_{Rot_1} (ps)	t_{Rot_2} (ps)	t_{Rot_3} (ps)	t_{Rot_1}/t_{Rot_2}	t_{Rot_1}/t_{Rot_3}
0.1	166.03 ± 3.25	56.39 ± 1.94	27.39 ± 0.36	2.95 ± 0.13	6.06 ± 0.15
1	167.82 ± 10.69	57.55 ± 2.23	27.86 ± 0.60	2.92 ± 0.27	6.03 ± 0.42
10	202.56 ± 19.47	63.57 ± 0.80	30.66 ± 0.29	3.19 ± 0.32	6.61 ± 0.64
100	387.75 ± 17.17	139.75 ± 10.47	69.19 ± 3.65	2.79 ± 0.24	5.61 ± 0.14

334 **4.3 Validation of Stokes-Einstein (SE) & Stokes-Einstein-Debye (SED) relations**

335 To achieve the same level of statistical precision with diffusion coefficient, it is estimated that
336 almost two orders of magnitude of trajectory durations are needed in viscosity calculation [23, 34].
337 Kinetic theory in liquid state which relates the diffusivity and viscosity by microscopic form of
338 friction coefficient has been regarded as a promising approach to obtain viscosity from diffusion
339 coefficient efficiently:

340 $$D = \frac{k_B T}{c_d}, \tag{19}$$

where c_d is the drag coefficient of molecule. In SE relation of molecule translational motion, $c_d=n\pi R_{eff}\eta$. In SED relation of molecule rotation motion, $c_d=n(\frac{4}{3}\pi R_{eff}^3)\eta$. Parameter n is equal to 4 or 6 based on slip or stick hydrodynamic boundary condition [14, 41], R_{eff} is effective molecule hydrodynamic radius.

Molecular rotation motion is characterised by molecular reorientation relaxation time $t_{Rot,}$ and D will only indicate self-diffusion coefficient of molecular translational motion in the following study. Conformational dynamics of molecule described by the longest relaxation time is in the form of:

$$t_{Rot} = \frac{c_d n_b^2 l^2}{3\pi^2 k_B T}. \quad (20)$$

SE and SED relation evolve into the following equations:

$$D = \frac{k_B T}{n_b c_d}, \quad (21)$$

$$t_{Rot} = \frac{12M\eta}{\pi^2 \rho RT}. \quad (22)$$

Here, c_d is the translational fractional drag coefficient of monomer, n_b is number of beads, l is effective bond length, R is gas constant, M is molecular mass. Elongated normal alkanes or polymer with Gaussian chain can be described by the Rouse model [19, 23, 45-47] where the molecular structure is treated as a collection of beads connected with a harmonic spring. For Gaussian polymer with linear chain, molecular geometry has the relation of $\langle R_{ee}^2\rangle=6\langle R_g^2\rangle=n_b l^2$, where R_{ee} is the end-to-end distance, R_g is gyration radius [46]. Combing Equations (20)-(22), eliminating c_d and subscribing l with R_{ee} or R_g, the viscosity *via* SE relation can be expressed as:

$$\eta(R_{ee}) = \frac{\rho RT\langle R_{ee}^2\rangle}{36MD}, \quad (23)$$

$$\eta(R_g) = \frac{\rho RT\langle R_g^2\rangle}{6MD}. \quad (24)$$

Viscosity *via* SED relation is the direct inversion of Equation (22) and is rewritten in the following form:

$$\eta(t_{Rot}) = \frac{\pi^2 \rho RT t_{Rot}}{12M}. \quad (25)$$

It was verified that normal alkane like HXD was too short to be regarded as a Gaussian chain [23, 46]. Moreover, the ester function group in MDC and MMR also reduce the Gaussianity indicating the breakdown of the Rouse model on methyl esters selected in this study. To use SE and SED relation in viscosity prediction of component with complexed molecular structure, obtaining R_{eff} is crucial. For Gaussian polymer, hydrodynamic radius can be obtained from ensemble-averaged estimates of the radius of gyration *via* R_{eff}=0.6647$<R_g^2>^{1/2}$ [48]. In temperature dependent transport property prediction, some previous studies on complexed non-Gaussian molecules like asphalt, ionic liquid or short alkane employed a linear regression between viscosity with single molecule property of translational diffusion coefficient or relaxation time, *i.e.*, $1/\eta \sim D/T$ or $t_{Rot}T \sim \eta$ [23, 33, 44, 49, 50]. More recently, R_{eff} is obtained by averaging molecule cross section over ensemble in EMD simulation. In conjunction with free volume theory of molecular diffusion, a parameter free and non-empirical method was proposed subsequently and was applied to predict viscosity of alkane lubricants over extreme pressure of 0.7 GPa. This indicates the applicability of SE relation in pressure dependent transport property prediction. The correlation of viscosity, translational diffusion and relaxation time is demonstrated in **Fig 7** in terms of MDC at 298.15 K (where different pressure values are indicated in (a) with colour schemes kept consistent in (a) and (b)). The linear scaling of transport property data is well-behaved, indicating the preservation of SE relation. Compared with the previous study by Shi *et al*. [51] on the coupling of instantaneous shear stress relaxation time with reorientation relaxation time, statistical error was eliminated significantly in this study due to the replicated trajectories. If we consider $\eta \sim t_{Rot} \sim 1/D$ overall, the product of relaxation time and diffusion coefficient, *i.e.* $t_{Rot} \cdot D$, should be constant if translation and rotation equally reflect viscosity [33, 49]. The relative standard deviation of translation-rotation diffusion product is also a small value of 5.06% at pressure ranging 1-100 MPa.

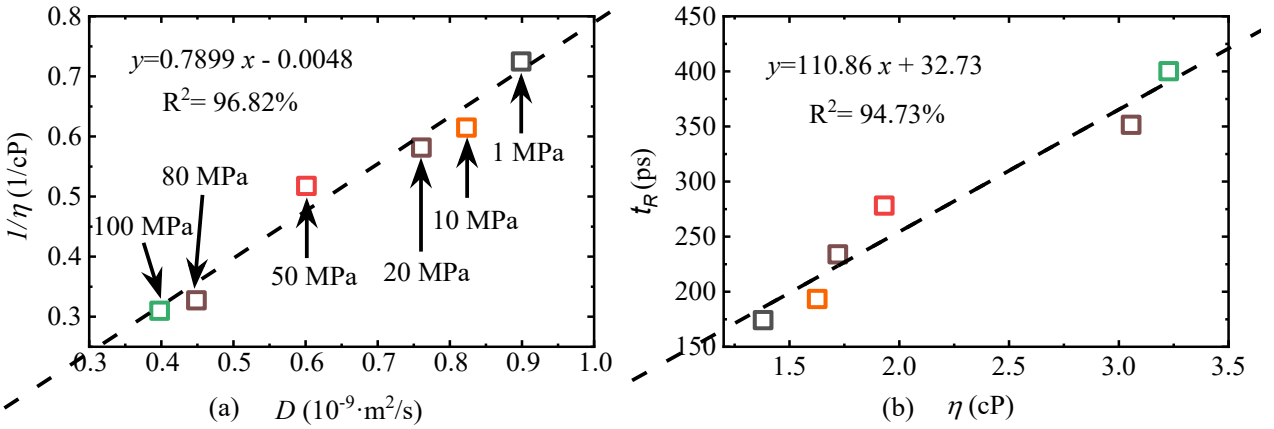

386

387 **Fig 7.** (a) Correlation between diffusion coefficient and the inverse of viscosity; (b) correlation
388 between relaxation time and viscosity; dashed lines indicate linear fitting; pressure is also indicated
389 by colour of the hollow square, and the colour code of pressure applies to the following plots of SE
390 relation.

391 **4.4 Evaluation of force field**

392 **4.4.1 Hydrodynamic radius**

393 In a previous EMD study on obtaining R_{eff} either *via* SE linear correlation or averaging
394 molecular cross section over ensemble, it was observed that R_{eff} remains universal with different
395 force fields of AA and UA models [15], and R_{eff} is only weakly dependent on density and temperature
396 [14]. Data of $1/\eta \sim D/T$ with pressure range of 10-300 MPa in isothermal conditions was plotted in **Fig**
397 **8** (with the same colour schemes as **Fig 7** for pressure). Viscosities of TDM results are used in the
398 Yeh-Hummer term of Equation (16) to correct system size effect on diffusion coefficient. The linear
399 regression worked well with different force fields and various isothermal temperatures. Compared
400 with the SE linear fitting in **Fig 7**, widen pressure range increased the goodness-of-fit. Slip boundary
401 conditions are employed in calculation of R_{eff}, which is the same boundary condition as Falk *et al.*
402 [14]. The conformation difference between MDC and MMR reflects merely the chain length
403 difference. Comparing the R_{eff} in **Fig 8**, effect of molecular structure on R_{eff} difference is distinguished.
404 This indicates that R_{eff} in EMD simulation is an intrinsic property of molecular structure and is

insensitive to the modelling configurations [52, 53].

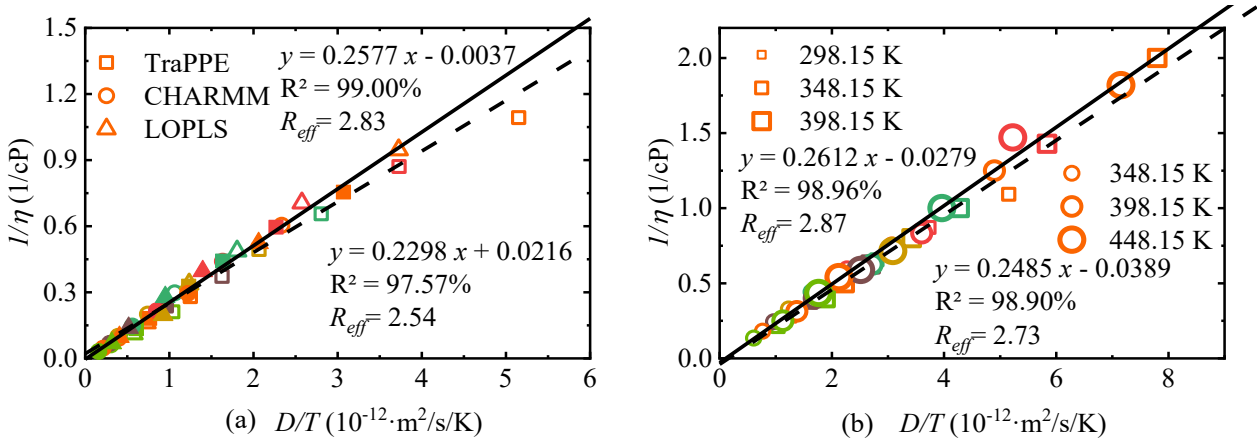

Fig 8. (a) Effect of force field on SE relation at 348.15 K with pressure ranging 10-300 MPa, where the hollow symbols and dashed line are results of MDC while solid symbols and solid line are results of MMR; (b) effect of temperature on SE relation, where the hollow square and dashed line are results of MDC while the hollow circle and solid line are results of MMR.

4.4.2 Physical properties

The capability of selected force fields was evaluated over density prediction of *n*-alkanes, considering the availability of the NIST data for comparison as shown in **Fig 9 (a)**. The densities of OTN, DCN and DDC are predicted at pressures ranging from 4 MPa to 100 MPa, and temperatures ranging from 300 K to 700 K. Densities of 361 phase points are calculated in total for each force field. Based on phase change data listed in **Table 1**, these conditions cover the gas phase, liquid phase and supercritical state. As shown in **Table 3**, there is no scaling effect of system size on density prediction, and statistical error is negligible. The simulation is performed in *NPT* ensemble containing 500 molecules, running 500 ps with density averaged over the last 200 ps trajectory.

Table 3. The density of MDC at 298.15 K and 0.1 MPa calculated using the TraPPE force field with different system sizes, results are averaged over 5 replicated independent trajectories.

Molecule number	125	250	500	1000	2000

ρ (g/ml)	0.8716	0.8714	0.8715	0.8714	0.8714
SD (g/ml)	5.67E-4	4.75E-4	2.08E-4	3.09E-4	6.97E-5

Among the three force fields, TraPPE reproduces densities most accurately with an average absolute relative deviation (AARD) of 1.44%, which is in agreement with previous MD simulations (AARD of 1% and 2% for DDC and *n*-Octacosane, respectively) [54]. Results of LOPLS has the largest AARD of 8.90%, despite that LOPLS parameters have been optimised over the dihedral energy profile and LJ interaction in gas phase [28]. Both CHARMM and LOPLS force fields show underestimation at low density conditions, particularly LOPLS which deviates around 10%-50% at low density conditions ranging from 0.5 g/ml to 0.3 g/ml. The prediction of these three force fields is accurate at liquid phase and high-pressure condensed phase at supercritical conditions.

Using the TraPPE force field for prediction, the densities of MDC and MMR at high pressure up to 300 MPa are shown in **Fig 9 (b)**. At 298.15 K, densities of MDC and MMR are limited up to 150 MPa and 50 MPa respectively to avoid the high-pressure induced liquid-solid transition [10]. The fitted density model itself is useful as a guide for the molecular modelling. The pressure dependence of density ρ is fitted by the Tait equation [55]:

$$\frac{\rho-\rho_{10}}{\rho} = A\log\left(\frac{B+P}{B+10}\right), \tag{26}$$

where ρ_{10} is the density at pressure of 10 MPa, A and B are the fitting parameters. From **Fig 9 (b)**, the density difference between MDC and MMR at 348.15 K appears at high pressure above 150 MPa.

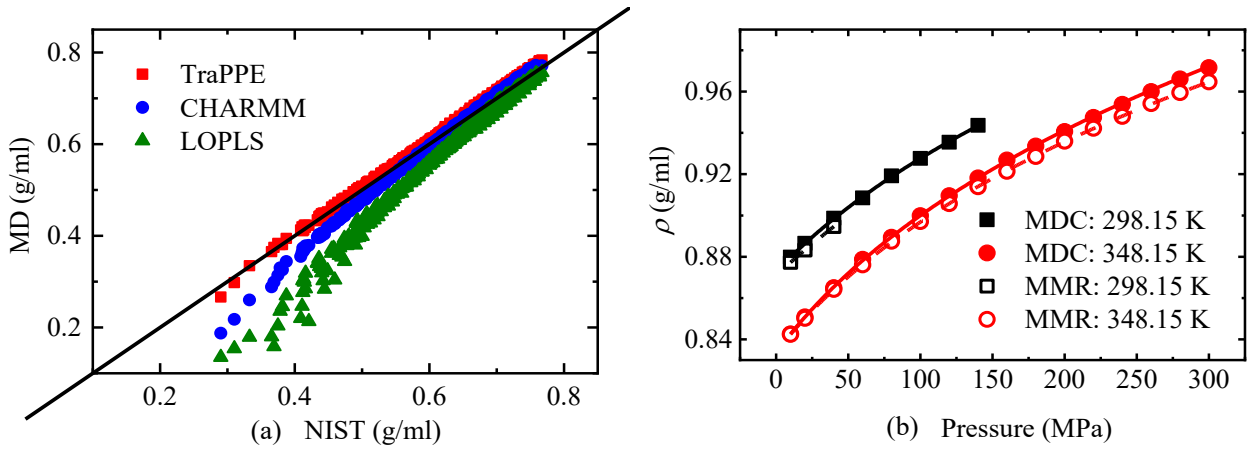

Fig 9. (a) Correlation between densities of NIST and results calculated by EMD simulation; (b) pressure effect on density of MDC and MMR at 298.15 K and 348.15 K, where lines are fitted results according to the Tait equation [55].

Diffusivity is difficult to obtain experimentally, with data rarely available. According to a previous study [28], the LOPLS force field exhibits improved accuracy on prediction of diffusion. This is also reflected in our simulation results shown in **Table 4**, *i.e.* LOPLS has the smallest deviation among the three force fields, with the value of -25.16% and -17.28% for DCN and DDC respectively. All atom molecular models of LOPLS and CHARMM tend to underestimate diffusion. Diffusion coefficient predicted by CHARMM was underestimated substantially by a factor of 0.63 and 0.54 for DCN and DDC respectively. Conversely, the united atom model of TraPPE overestimates the diffusion because the absence of hydrogen atoms increases the molecule free volume [39]. Diffusion constant is dependent on molecular size, while all these three force fields followed exactly the scaling law of diffusivity over molecular size, *i.e.*, $D \propto M^{-2}$ [56, 57]. Scaling factors of D_{DDC}/D_{CCN} are equal to 0.63, 0.57, and 0.58 respectively for TraPPE, CHARMM and LOPLS.

Table 4. Comparison of diffusion coefficient with the experimental result at 298.15 K and 0.1 MPa (10^{-9} m^2/s); data was corrected over system size effect.

	Expt.	TraPPE	CHARMM	LOPLS
DCN	1.55 [58]	2.35 ± 0.15	0.83 ± 0.062	1.16 ± 0.047
DDC	0.81 [59]	1.47 ± 0.059	0.47 ± 0.019	0.67 ± 0.030

Considering the temperature range in the experimental result, viscosities of MDC and MMR are calculated at isotherms of 298.15 K and 348.15 K *via* TDM. The comparison of viscosity-pressure results is shown in **Fig 10**. The corresponding experimental values are adopted from the work of Habrioux *et al*. [4, 5], where isothermal viscosities are correlated according to the modified Tait equation:

$$\ln\left(\frac{\eta}{\eta_{0.1}}\right) = A(P-0.1) + B\ln\left(\frac{C+(P-0.1)}{C}\right), \quad (27)$$

where A, B and C are fitting parameters. A is temperature independent, B and C are fluid specific parameters dependent on temperature [4, 5, 9], $\eta_{0.1}$ is the viscosity at 0.1 MPa for each isothermal temperature which can be obtained by fitting the Vogel-Fulcher-Tammann correlation in the form of

$$\eta_{0.1}(T) = A\exp\left(\frac{B}{T-C}\right), \quad (28)$$

where A, B and C are fitting parameters.

For MD simulation, the viscosity-pressure relation is described by the single exponential Barus model [60] given as:

$$\eta = \eta_0 \exp(AP), \quad (29)$$

where η_0 is zero pressure viscosity, A is fitting parameter. Equation (29) has been used to successfully describe the rheology of 1-diphenylethane at high pressure up to 400 MPa [15].

All these three force fields can describe the viscosity-pressure trend. It is observed that CHARMM overestimates viscosity substantially in all conditions, and TraPPE underestimates viscosity. The deviation is more prominent at high-pressure compressed condition. LOPLS exhibits the best agreement with experimental values. The evaluation of force field performance using EMD-TDM method is consistent with the previous observation using NEMD simulation with periodic perturbation method [54].

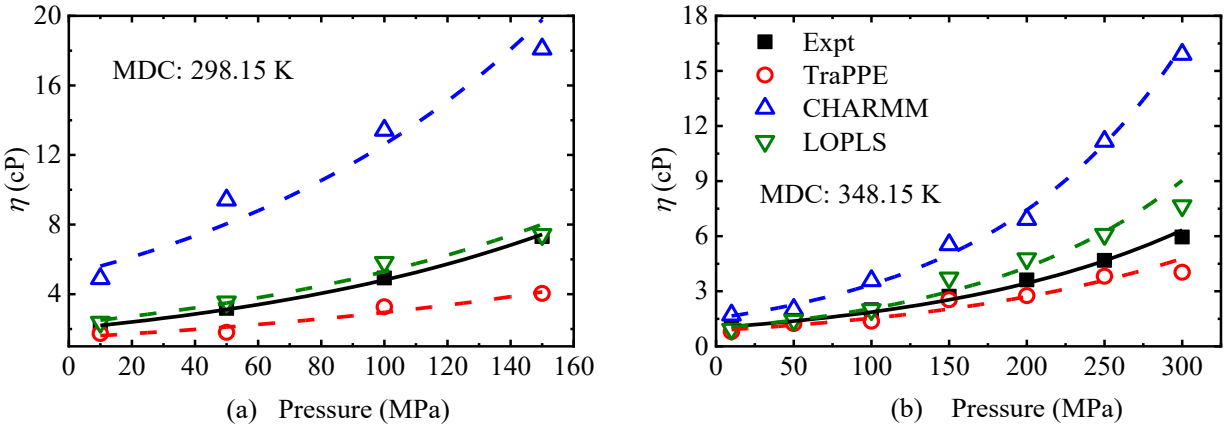

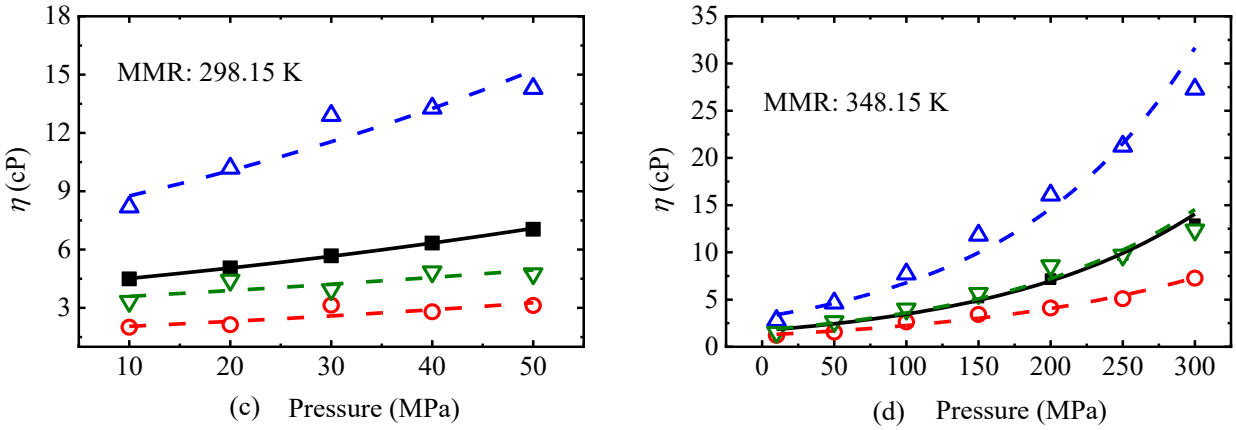

Fig 10. Comparison of viscosity between MD simulation and experimental results, where solid lines are experimental results, and dashed lines are MD results fitted according to the Barus model [60].

5 Discussion

5.1 Breakdown of SE relation due to high-pressure solidification

A violation or breakdown of SE relation has been observed in viscous liquids due to the occurrence of glass-formation instead of normal crystallization when liquid is cooled sufficiently fast. Decoupling between D and η would occur in supercooled liquids when temperature is below approximately $1.2T_g$ (T_g is glass transition temperature) [61, 62]. Correspondingly, the observations of the high-pressure glass formation of water [63], ionic liquid [64] and crude oil [65], raise a question on whether SE remains valid for liquids which are densified by high pressure instead of cooling [14]. Some experimental studies confirmed the liquid-solid transition of polyatomic organic components, *e.g.*, solidification of biodiesel mixtures (up to 350 MPa) [12], *n*-Octane (~0.9 GPa) [66], pure FAMEs [10] (up to 80 MPa), *n*-Tetradecane (302.8 MPa) [67], and the crystallisation of Methyl Stearate (0.2 GPa) [11]. The MD modelling and simulation may be used to understand the phenomenon and answer the question.

To scrutinise the high-pressure induced phase transition of FAMEs, we firstly tracked the morphology evolution of the modelling system in 100 ns trajectory. Molecular alignment was

quantified by using a collective variable named SMAC (Solid Molecule Angle Criteria), in which the relative orientation is characterised by torsion angle between internal molecule vector. The SMAC variable describes the local order in the neighbourhood of a molecule, and has been used to study the phase transition such as the nucleation process of urea [68] and the crystallisation of paraffin in cooling condition [69]. The SMAC is expressed as:

$$s_i = \frac{\left\{1-\psi\left(\sum_{j\neq i}^{N}\sigma(r_{ij})\right)\right\}\sum_{j\neq i}^{N}\sigma(r_{ij})\sum_n K_n\left(\phi_{ij}\right)}{\sum_{j\neq i}^{N}\sigma(r_{ij})}, \quad (30)$$

where r_{ij} is the distance between centre of vector of molecule i and j, ϕ_{ij} is torsion angle between the molecular vectors, $\sigma(r_{ij})$ is a switching function to ensure that only molecules within the cut-off distance are considered, ψ is also a switching function, K_n is a kernel function consisted of two Gaussian functions with standard deviation of 0.48 and reference angles of zero and π [68-70]. $K_n(\phi_{ij})$ converts torsion angles close to zero and π to a number close to one which corresponds to ordered arrangement of molecules in MD system [70]. $\sigma(r_{ij})$ is a rational function expressed as:

$$\sigma = \frac{1-\left(\frac{r-d_0}{r_0}\right)^n}{1-\left(\frac{r-d_0}{r_0}\right)^m}, \quad (31)$$

where d_0=0.0, n=6, m=2n, r_0 is cut-off distance equal to 8.6 Å which is the radius of second coordination sphere obtained by radial distribution function of molecule.

Compared with MDC and alkanes in **Table 1**, MMR has the highest melting temperature of 291.24 K, and was selected in favour of liquid-solid transition in MD simulation. The time evolution of the collective variable and typical morphology snapshots of MMR are shown in **Fig 11**. Normally, FAMEs melting temperature increases with increasing pressure [10]. At conditions of 298.15 K - 50 MPa and 348.15 K - 300 MPa, collective variables are stable and have relatively low values as shown in **Fig 11 (a)**. The time invariance indicates the unchanged amorphous liquid states at these conditions. Solidification process of MMR at 298.15 K - 100 MPa can be described by three different stages. Molecular rearrangement takes place before 10 ns with SMAC increasing from 0.42 to 0.47, which

is followed by accelerated solidification process with SMAC increasing further to 0.7 in 20 ns. After 30 ns, SMAC resides at the plateau and remains stable with MD system changed into the heterogeneous structure as shown in **Fig 11 (b)**. It should be noted that time evolution of SMAC in **Fig 11 (a)** shows the approximate trend with the nucleation of pure paraffin under harsh subcooling conditions [69]. This indicates that high pressure is supposed to have the equivalent effect on FAME crystallisation behaviour with the cooling process.

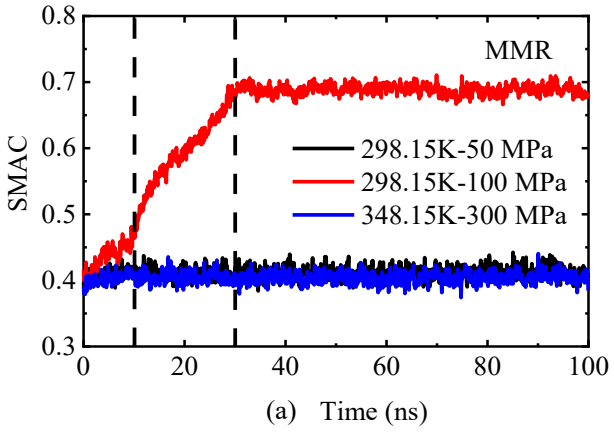

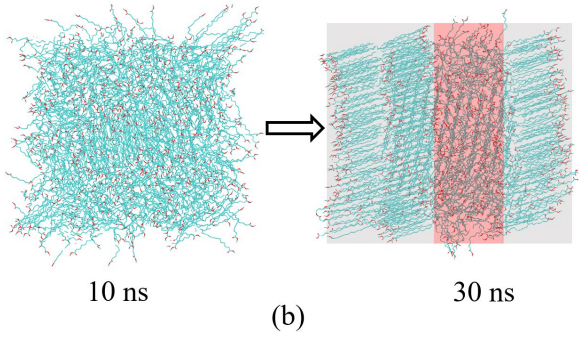

Fig 11. (a) The SMAC parameter of MMR at different temperatures and pressures, where black dashed lines indicate transition time of 298.15 K - 100 MPa; (b) snapshots of MMR MD system at 298.15 K - 100 MPa, where grey area indicates ordered alignment of solid nuclei while red area indicates amorphous liquid phase.

The mechanism of SE violation of liquids has been attributed to the attained solidity upon supercooling, which is in accord with the growth of non-Gaussianity and spatially heterogeneous dynamics [62, 71]. The high-pressure induced heterogeneity is reflected in the spatial distribution of

solid-liquid phase as shown in **Fig 11 (b)**. Pressure effect on MMR molecular conformation is characterised by the end-to-end distance probability distribution as shown in **Fig 12**. There are two peak values of probability, at 1.67 nm and 1.89 nm, corresponding to liquid and solid state respectively. The probability at 50 MPa liquid state is not exactly a normal distribution because MMR is not ideal Gaussian polymer chain. After crystallisation at 100 MPa, the peak value shifts to 1.89 nm and probability increases with solidification degree accordingly. This indicates that high-pressure solidification can also enhance the non-Gaussian behaviour of MMR.

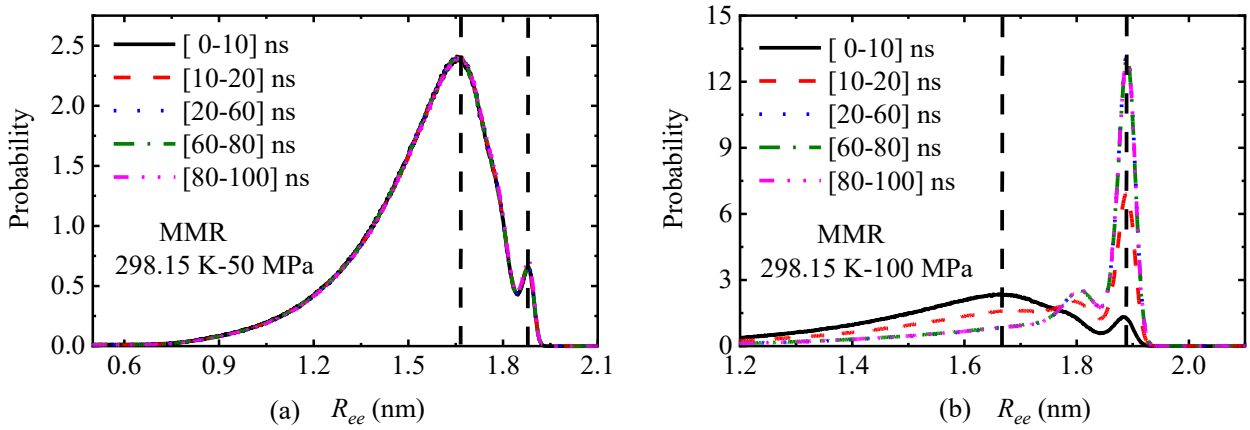

Fig 12. Probability distribution of MMR molecule end-to-end distance at 298.15 K, where the probability is the statistical results in the time interval, and the black dashed lines indicate the peak values; lines of [20-60] ns, [60-80] ns and [80-100] ns in (b) are overlapped.

In glass transition of supercooled liquids, dynamics like structural relaxation time in different regions only a few manometers away can differ orders of magnitude [50]. In high-pressure solidified systems displayed in **Fig 11 (b)**, molecule in solid phase is stretched while in liquid phase it is flexible. The heterogeneous spatial distribution of molecule conformation indicates the structure relaxation dynamics and molecular mobility is also highly spatially correlated. The time evolution of overall diffusion coefficient is shown in **Fig 13**. Different with the stable values at 50 MPa, diffusion coefficient at 100 MPa shows an inverse relation with the solidification degree. It reached an extremely low average value of 9.68×10^{-11} m^2/s at final stage where stretched molecule at solid region

would slide in preferred direction along the main chain [15]. Once diffusion falls below the cut-off value (5×10^{-11} m^2/s for argon), pressure-induced glass transition occurs [72].

Viscosity becomes large due to the extraordinary slow-down of stress relaxation when temperature gets close to T_g [61, 73]. For solidified high-pressure system, it is impracticable to obtain the viscosity directly using TDM, because at least 30 ns equilibrium run is needed before data collection. Moreover, feasibility of the GK method is questionable in a heterogeneous system. Previous MD modelling study on 1-methylnaphthalene implied that the high-pressure induced vitrification would occur above 300 MPa which explained the observation of faster-than-exponential growth of viscosity with pressure [17].

To investigate phase transition in cooling of pure and spatially unconfined liquids, it is necessary to perform simulation with long time scale due to the large number of possible network configurations [74]. Considerable long time trajectory is also needed to study the violation/preservation of SE relation. The application of EMD has been common in studying tribology of lubricants in high-pressure conditions up to 1 GPa [14, 16], where the appearance of solid nuclei is possible. It should be stressed that identifying the conditions where spatial heterogeneities occur is vital for the reliability in predicting high-pressure transport properties.

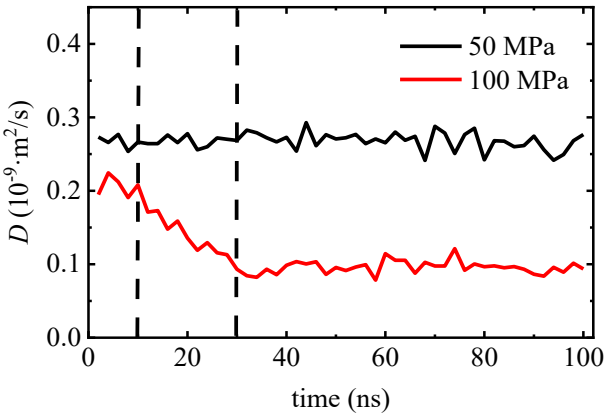

Fig 13. Time evolution of overall diffusion coefficient of MMR at 298.15 K, where trajectories are partitioned every 2 ns, and diffusion coefficient is the linear fitting of MSD between 200 ps and 1800

ps within each time interval; black dashed lines indicate the transition time of 100 MPa.

5.2 Crossing the SE relation

In general, viscosity is a mesoscopic property which is experimentally measurable while diffusion coefficient is a microscopic description of molecular motion which can be readily obtained in EMD simulation. However, direct viscosity measurements for every fluid at all conditions of interest are not only expensive and time-consuming but also extremely difficult and sometimes impossible to obtain especially at high-temperature, high-pressure (HTHP) conditions. The work of Falk *et al*. [14], Kondratyuk *et al*. [15] and Gordon [52, 53] proved that R_{eff} is a constant parameter over a wide range of HTHP conditions. It demonstrated that predicting viscosity through diffusion coefficient *via* scaling behaviour of SE relation is promising in both reducing computational cost and keeping the ultimate accuracy.

Hereon, we propose a predictive method *via* the crossover linkage between experimentally available viscosities and corresponding EMD diffusion coefficients in any force field as shown in **Fig 14**. Using the hybrid R_{eff} *via* liner regression, the viscosity can be estimated in HTHP region after extrapolation provided SE relation preserves. The predicted value should have experimental-level accuracy. Among these three force fields, TraPPE is supposed to be robust even in extreme conditions considering the overall capability in density prediction over a wide range of HTHP conditions. The demonstrated correlations between viscosity and diffusion coefficient can be exploited in the determination of transport properties of new fluids such as new fuels or those of existing fluids/fuels in unexplored HTHP supercritical conditions.

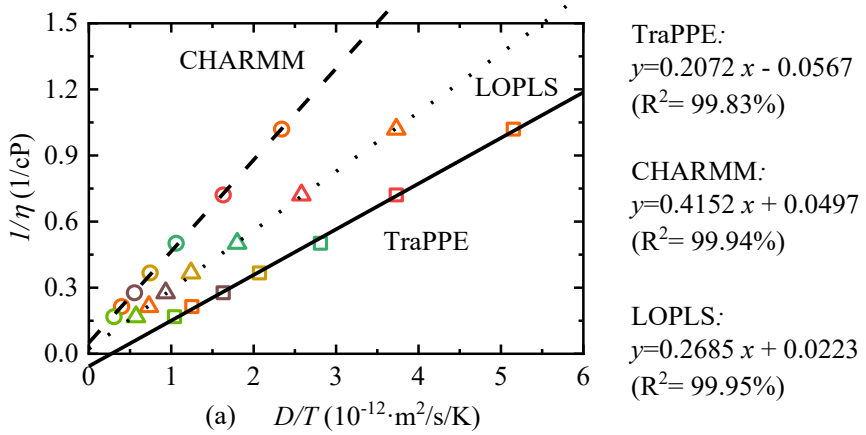

592

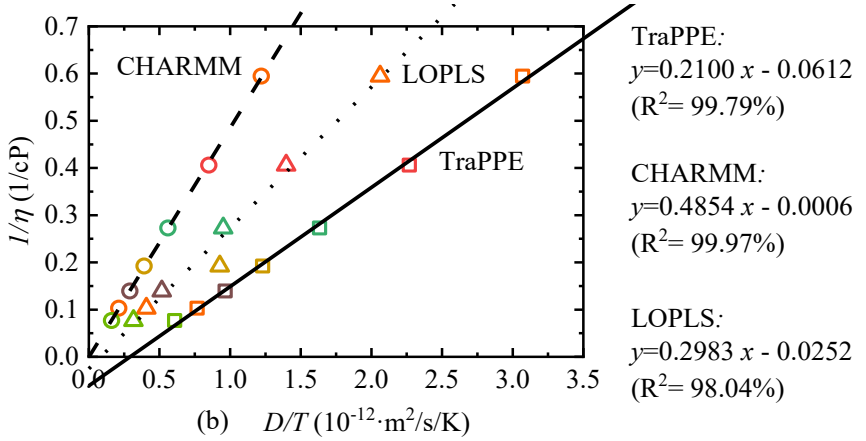

593

594 **Fig 14.** Correlation between viscosity from experiment and diffusion coefficient from EMD
595 simulation at temperature 348.15 K: (a)-MDC; (b)-MMR. Solid line is the fitting of TraPPE, dashed
596 line is the fitting of CHARMM and dotted line is the fitting of LOPLS.

597 ## 6 Conclusion

598 In this study, equilibrium molecular modelling with three force fields (TraPPE, CHARMM and
599 LOPLS) has been performed to comprehensively study the properties of FAMEs in high-pressure
600 conditions up to 300 MPa, which is very challenging for other methods such as experimental
601 measurements. This study provided a new methodological approach to fuel property predictions in
602 extreme conditions using molecular dynamics simulation, with results given in terms of transport
603 property predictions, together with analyses of the dynamics of molecular structure and Stokes-
604 Einstein relation. There are several observations from the simulation and the methodological

605 approach.

606 Determining the plateau time for FAME viscosity is a trade-off due to the increasing statistical
607 error with longer time range for the running integral. Averaging over replicated independent
608 trajectories with subsequent fitting is a feasible solution to obtain viscosity rigorously in spite of the
609 increased computational cost. Translational diffusion coefficient obtained *via* Einstein method is
610 statistically accurate, and scaling effect of system size should be considered. Rotational diffusion is
611 characterised *via* reorientation relaxation time of the end-to-end vector.

612 Accuracy of density, diffusion coefficient and viscosity prediction varies among the three force
613 fields. TraPPE force field shows a very close agreement with the experimental density over a wide
614 range of conditions. All-atom models tend to underestimate diffusion and overestimate viscosity,
615 while the united atom model shows an opposite trend. LOPLS force field has performed better than
616 CHARMM on diffusion coefficient and viscosity.

617 The Stokes-Einstein relation holds for most conditions where diffusion coefficient, relaxation
618 time and viscosity are correlated, except at temperatures close to the melting point with high pressure.
619 There is a need to pay special attention on this when using EMD to predict transport properties at
620 extreme high pressures. Because high pressure induced solidification requires simulation with long
621 time scale for the nuclei to appear, the consequent spatial heterogeneity results in the breakdown of
622 Stokes-Einstein relation.

623 A hybrid effective hydrodynamic radius is obtained by the cross-correlation of experimental
624 viscosities and EMD diffusion coefficients. The predictive method established in this study can be
625 used to estimate viscosity in high-temperature and high-pressure conditions from the corresponding
626 EMD diffusion coefficient provided that Stokes-Einstein relation applies.

627 # 7 References

628 [1] C. Chen, L. Cai, L. Zhang, W. Fu, Y. Hong, X. Gao, *et al*. Transesterification of rice bran oil

to biodiesel using mesoporous NaBeta zeolite-supported molybdenum catalyst: experimental and kinetic studies. Chemical Engineering Journal. 2020;382:122839.

[2] L. Lin, M.A. Kedzierski. Density and viscosity of a polyol ester lubricant: Measurement and molecular dynamics simulation. International Journal of Refrigeration. 2020;118:188-201.

[3] K.R. Bukkarapu, A. Krishnasamy. A critical review on available models to predict engine fuel properties of biodiesel. Renewable and Sustainable Energy Reviews. 2021:111925.

[4] M. Habrioux, J.-P. Bazile, G. Galliero, J.L. Daridon. Viscosities of fatty acid methyl and ethyl esters under high pressure: methyl caprate and ethyl caprate. Journal of Chemical & Engineering Data. 2015;60:902-908.

[5] M. Habrioux, J.-P. Bazile, G. Galliero, J.L. Daridon. Viscosities of fatty acid methyl and ethyl esters under high pressure: methyl myristate and ethyl myristate. Journal of Chemical & Engineering Data. 2016;61:398-403.

[6] NIST Chemistry WebBook https://webbook.nist.gov/chemistry/fluid/.

[7] F.R. do Carmo, N.S. Evangelista, F.A. Fernandes, H.B. de Sant'Ana. Evaluation of optimal methods for critical properties and acentric factor of biodiesel compounds with their application on soave–redlich–kwong and peng–robinson equations of state. Journal of Chemical & Engineering Data. 2015;60:3358-3381.

[8] N.W.M. Zulkifli, S. Azman, M. Kalam, H.H. Masjuki, R. Yunus, M. Gulzar. Lubricity of bio-based lubricant derived from different chemically modified fatty acid methyl ester. Tribology International. 2016;93:555-562.

[9] H.O. Baled, I.K. Gamwo, R.M. Enick, M.A. McHugh. Viscosity models for pure hydrocarbons at extreme conditions: A review and comparative study. Fuel. 2018;218:89-111.

[10] A.C. Kouakou, K. Le Mapihan, J. Pauly. Solid–liquid equilibria under high pressure of pure fatty acid methyl esters. Fuel. 2013;109:297-302.

[11] X. Liu, C. Bull, A. Kleppe, P. Dowding, K. Lewtas, C. Pulham. High-pressure crystallisation studies of biodiesel and methyl stearate. CrystEngComm. 2019;21:4427-4436.

[12] R. Tarakowski, A. Malanowski, A.J. Rostocki, M. Kowalczyk, P. Modzelewski, S. Ptasznik, *et al*. Could RME biodiesel be potentially harmful to modern engine? solidification process in RME. Fuel. 2015;146:28-32.

[13] X. Nie, Z. Du, L. Zhao, S. Deng, Y. Zhang. Molecular dynamics study on transport properties of supercritical working fluids: Literature review and case study. Applied Energy. 2019;250:63-80.

[14] K. Falk, D. Savio, M. Moseler. Nonempirical free volume viscosity model for alkane lubricants under severe pressures. Physical Review Letters. 2020;124:105501.

[15] N. Kondratyuk, D. Lenev, V. Pisarev. Transport coefficients of model lubricants up to 400 MPa from molecular dynamics. The Journal of Chemical Physics. 2020;152:191104.

[16] N.D. Kondratyuk, V.V. Pisarev. Calculation of viscosities of branched alkanes from 0.1 to 1000 MPa by molecular dynamics methods using COMPASS force field. Fluid Phase Equilibria. 2019;498:151-159.

[17] N.D. Kondratyuk, V.V. Pisarev, J.P. Ewen. Probing the high-pressure viscosity of hydrocarbon mixtures using molecular dynamics simulations. The Journal of Chemical Physics. 2020;153:154502.

[18] Y. Wang, S. Gong, L. Li, G. Liu. Sub-to-supercritical properties and inhomogeneity of JP-10 using molecular dynamics simulation. Fuel. 2021;288:119696.

[19] X. Yang, M. Zhang, Y. Gao, J. Cui, B. Cao. Molecular dynamics study on viscosities of sub/supercritical n-decane, n-undecane and n-dodecane. Journal of Molecular Liquids. 2021;335:116180.

[20] K. Chae, P. Elvati, A. Violi. Effect of molecular configuration on binary diffusion coefficients of linear alkanes. The Journal of Physical Chemistry B. 2011;115:500-506.

[21] K. Chae, A. Violi. Mutual diffusion coefficients of heptane isomers in nitrogen: A molecular dynamics study. The Journal of Chemical Physics. 2011;134:044537.

[22] E.J. Maginn, R.A. Messerly, D.J. Carlson, D.R. Roe, J.R. Elliott. Best practices for computing transport properties 1. Self-diffusivity and viscosity from equilibrium molecular dynamics [article v1. 0]. Living Journal of Computational Molecular Science. 2018;1:6324.

[23] M. Mondello, G.S. Grest. Viscosity calculations of n-alkanes by equilibrium molecular dynamics. The Journal of Chemical Physics. 1997;106:9327-9336.

[24] G. Pranami, M.H. Lamm. Estimating error in diffusion coefficients derived from molecular dynamics simulations. Journal of Chemical Theory and Computation. 2015;11:4586-4592.

[25] M.G. Martin, J.I. Siepmann. Transferable potentials for phase equilibria. 1. United-atom description of n-alkanes. The Journal of Physical Chemistry B. 1998;102:2569-2577.

[26] K. Vanommeslaeghe, E. Hatcher, C. Acharya, S. Kundu, S. Zhong, J. Shim, *et al*. CHARMM general force field: A force field for drug-like molecules compatible with the CHARMM all-atom additive biological force fields. Journal of Computational Chemistry. 2010;31:671-690.

[27] W.L. Jorgensen, D.S. Maxwell, J. Tirado-Rives. Development and testing of the OPLS all-atom force field on conformational energetics and properties of organic liquids. Journal of the American Chemical Society. 1996;118:11225-11236.

[28] S.W. Siu, K. Pluhackova, R.A. Böckmann. Optimization of the OPLS-AA force field for long hydrocarbons. Journal of Chemical Theory and Computation. 2012;8:1459-1470.

[29] K. Pluhackova, H. Morhenn, L. Lautner, W. Lohstroh, K.S. Nemkovski, T. Unruh, *et al*. Extension of the LOPLS-AA force field for alcohols, esters, and monoolein bilayers and its validation by neutron scattering experiments. The Journal of Physical Chemistry B. 2015;119:15287-15299.

[30] J. Huang, A.D. MacKerell Jr. CHARMM36 all-atom additive protein force field: Validation based on comparison to NMR data. Journal of Computational Chemistry. 2013;34:2135-2145.

[31] G. Kamath, J. Robinson, J.J. Potoff. Application of TraPPE-UA force field for determination of vapor-liquid equilibria of carboxylate esters. Fluid Phase Equilibria. 2006;240:46-55.

[32] D. Van Der Spoel, E. Lindahl, B. Hess, G. Groenhof, A.E. Mark, H.J. Berendsen. GROMACS: fast, flexible, and free. Journal of Computational Chemistry. 2005;26:1701-1718.

[33] L. Zhang, M.L. Greenfield. Relaxation time, diffusion, and viscosity analysis of model asphalt systems using molecular simulation. The Journal of Chemical Physics. 2007;127:194502.

[34] Y. Zhang, A. Otani, E.J. Maginn. Reliable viscosity calculation from equilibrium molecular dynamics simulations: A time decomposition method. Journal of Chemical Theory and Computation. 2015;11:3537-3546.

[35] K.-S. Kim, M.H. Han, C. Kim, Z. Li, G.E. Karniadakis, E.K. Lee. Nature of intrinsic uncertainties in equilibrium molecular dynamics estimation of shear viscosity for simple and complex fluids. The Journal of Chemical Physics. 2018;149:044510.

[36] V. Brazhkin, Y.D. Fomin, A. Lyapin, V. Ryzhov, E. Tsiok, K. Trachenko. “Liquid-gas” transition in the supercritical region: Fundamental changes in the particle dynamics. Physical Review Letters. 2013;111:145901.

[37] S. Bellissima, M. Neumann, E. Guarini, U. Bafile, F. Barocchi. Density of states and dynamical crossover in a dense fluid revealed by exponential mode analysis of the velocity autocorrelation function. Physical Review E. 2017;95:012108.

[38] C. Scalliet, A. Gnoli, A. Puglisi, A. Vulpiani. Cages and anomalous diffusion in vibrated dense granular media. Physical Review Letters. 2015;114:198001.

[39] N.D. Kondratyuk, G.E. Norman, V.V. Stegailov. Self-consistent molecular dynamics calculation of diffusion in higher n-alkanes. The Journal of Chemical Physics. 2016;145:204504.

[40] A.T. Celebi, S.H. Jamali, A. Bardow, T.J. Vlugt, O.A. Moultos. Finite-size effects of diffusion coefficients computed from molecular dynamics: a review of what we have learned so far. Molecular Simulation. 2020:1-15.

[41] O.A. Moultos, Y. Zhang, I.N. Tsimpanogiannis, I.G. Economou, E.J. Maginn. System-size corrections for self-diffusion coefficients calculated from molecular dynamics simulations: The case of CO2, n-alkanes, and poly (ethylene glycol) dimethyl ethers. The Journal of Chemical Physics. 2016;145:074109.

731 [42] I.-C. Yeh, G. Hummer. System-size dependence of diffusion coefficients and viscosities
732 from molecular dynamics simulations with periodic boundary conditions. The Journal of Physical
733 Chemistry B. 2004;108:15873-15879.
734 [43] T.J. dos Santos, C.R. Abreu, B.A. Horta, F.W. Tavares. Self-diffusion coefficients of
735 methane/n-hexane mixtures at high pressures: An evaluation of the finite-size effect and a comparison
736 of force fields. The Journal of Supercritical Fluids. 2020;155:104639.
737 [44] D.D. Li, M.L. Greenfield. Viscosity, relaxation time, and dynamics within a model asphalt
738 of larger molecules. The Journal of Chemical Physics. 2014;140:034507.
739 [45] M. Doi, S.F. Edwards, S.F. Edwards. The theory of polymer dynamics: Oxford University
740 press; 1988.
741 [46] M. Mondello, G.S. Grest, E.B. Webb III, P. Peczak. Dynamics of n-alkanes: Comparison to
742 Rouse model. The Journal of Chemical Physics. 1998;109:798-805.
743 [47] K. Kremer, G.S. Grest. Dynamics of entangled linear polymer melts: A molecular-dynamics
744 simulation. The Journal of Chemical Physics. 1990;92:5057-5086.
745 [48] K. Haydukivska, V. Blavatska, J. Paturej. Universal size ratios of Gaussian polymers with
746 complex architecture: radius of gyration vs hydrodynamic radius. Scientific Reports. 2020;10:1-11.
747 [49] L. Zhang, M.L. Greenfield. Rotational relaxation times of individual compounds within
748 simulations of molecular asphalt models. The Journal of Chemical Physics. 2010;132:184502.
749 [50] T. Koddermann, R. Ludwig, D. Paschek. On the validity of Stokes-Einstein and Stokes-
750 Einstein-Debye relations in ionic liquids and ionic-liquid mixtures. ChemPhysChem. 2008;9:1851.
751 [51] Z. Shi, P.G. Debenedetti, F.H. Stillinger. Relaxation processes in liquids: Variations on a
752 theme by Stokes and Einstein. The Journal of Chemical Physics. 2013;138:12A526.
753 [52] P.A. Gordon. Extrapolation of Rheological Properties for Lubricant Components with
754 Stokes-Einstein Relationships. Industrial & Engineering Chemistry Research. 2005;44:5828-5835.
755 [53] P.A. Gordon. Characterizing Isoparaffin Transport Properties with Stokes-Einstein
756 Relationships. Industrial & Engineering Chemistry Research. 2003;42:7025-7036.
757 [54] K.D. Papavasileiou, L.D. Peristeras, A. Bick, I.G. Economou. Molecular dynamics
758 simulation of pure n-alkanes and their mixtures at elevated temperatures using atomistic and coarse-
759 grained force fields. The Journal of Physical Chemistry B. 2019;123:6229-6243.
760 [55] J. Dymond, R. Malhotra. The Tait equation: 100 years on. International Journal of
761 Thermophysics. 1988;9:941-951.
762 [56] E. Von Meerwall, S. Beckman, J. Jang, W. Mattice. Diffusion of liquid n-alkanes: Free-
763 volume and density effects. The Journal of Chemical Physics. 1998;108:4299-4304.
764 [57] D.E. Freed, L. Burcaw, Y.-Q. Song. Scaling laws for diffusion coefficients in mixtures of

765 alkanes. Physical Review Letters. 2005;94:067602.
766 [58] J.W. Moore, R.M. Wellek. Diffusion coefficients of n-heptane and n-decane in n-alkanes
767 and n-alcohols at several temperatures. Journal of Chemical and Engineering data. 1974;19:136-140.
768 [59] M.H.S.H.A. Sacco. Temperature-dependent self-diffusion coefficients of water and six
769 selected molecular liquids for calibration in accurate ^{1}H NMRPFG measurements. Physical
770 Chemistry Chemical Physics. 2000;2:4740-4742.
771 [60] J. Dench, L. Di Mare, N. Morgan, J. Wong. Comparing the molecular and global rheology
772 of a fluid under high pressures. Physical Chemistry Chemical Physics. 2018;20:30267-30280.
773 [61] P.G. Debenedetti, F.H. Stillinger. Supercooled liquids and the glass transition. Nature.
774 2001;410:259-267.
775 [62] T.G. Lombardo, P.G. Debenedetti, F.H. Stillinger. Computational probes of molecular
776 motion in the Lewis-Wahnström model for *ortho*-terphenyl. The Journal of Chemical Physics.
777 2006;125:174507.
778 [63] O. Andersson. Glass-liquid transition of water at high pressure. Proceedings of the National
779 Academy of Sciences. 2011;108:11013-11016.
780 [64] M.C. Ribeiro, A.A. Pádua, M.F.C. Gomes. Glass transition of ionic liquids under high
781 pressure. The Journal of Chemical Physics. 2014;140:244514.
782 [65] V. Kutcherov, A. Chernoutsan, V. Brazhkin. Crystallization and glass transition in crude oils
783 and their fractions at atmospheric and high pressures. Journal of Molecular Liquids. 2017;241:428-
784 434.
785 [66] T. Takekiyo, Y. Koyama, K. Matsuishi, Y. Yoshimura. High-Pressure Raman Study of n-
786 Octane up to 15 GPa. The Journal of Physical Chemistry B. 2020;124:11189-11196.
787 [67] X. Jian, H. Zheng. Raman scattering spectroscopic study of n-tetradecane under high
788 pressure and ambient temperature. Spectrochimica Acta Part A: Molecular and Biomolecular
789 Spectroscopy. 2009;72:214-217.
790 [68] F. Giberti, M. Salvalaglio, M. Mazzotti, M. Parrinello. Insight into the nucleation of urea
791 crystals from the melt. Chemical Engineering Science. 2015;121:51-59.
792 [69] G.C. da Silva, F.G. Oliveira, W.F. de Souza, M.C. de Oliveira, P.M. Esteves, B.A. Horta.
793 Effects of paraffin, fatty acid and long alkyl chain phenol on the solidification of n-hexadecane under
794 harsh subcooling condition: A molecular dynamics simulation study. Fuel. 2021;285:119029.
795 [70] G.A. Tribello, F. Giberti, G.C. Sosso, M. Salvalaglio, M. Parrinello. Analyzing and driving
796 cluster formation in atomistic simulations. Journal of Chemical Theory and Computation.
797 2017;13:1317-1327.
798 [71] T. Kawasaki, K. Kim. Identifying time scales for violation/preservation of Stokes-Einstein

799 relation in supercooled water. Science Advances. 2017;3:e1700399.
800 [72] S.L. Shumway, A.S. Clarke, H. Jónsson. Molecular dynamics simulations of a pressure-
801 induced glass transition. The Journal of Chemical Physics. 1995;102:1796-1805.
802 [73] M. Ediger, P. Harrowell. Perspective: Supercooled liquids and glasses. The Journal of
803 Chemical Physics. 2012;137:080901.
804 [74] M. Matsumoto, S. Saito, I. Ohmine. Molecular dynamics simulation of the ice nucleation
805 and growth process leading to water freezing. Nature. 2002;416:409-413.
806